International Journal of Hydrogen Energy 100 (2025) 214–221

Contents lists available at ScienceDirect

International Journal of Hydrogen Energy

journal homepage: www.elsevier.com/locate/he

Iridium nanoparticles for oxygen evolution reaction on carbon and TiO_2 supports from a Raman perspective

Leonard Moriau [a], Ivan Marić [b,1], Marjan Bele [a], Anja Logar [a], Nejc Hodnik [a], Angelja K. Surca [a,*]

[a] National Institute of Chemistry, Hajdrihova 19, 1000, Ljubljana, Slovenia
[b] Centre of Excellence for Low Carbon Technologies, Hajdrihova 19, 1000 Ljubljana, Slovenia

ARTICLE INFO

Handling Editor: Umit Demirci

Keywords:
Iridium
Carbon support
TiO_2 support
OER activity
Raman spectroscopy
Electrocatalyst
Thermal annealing

ABSTRACT

Ir-based electrocatalysts are crucial for oxygen evolution reaction (OER) in acidic media. Herein, the OER activity of Ir nanoparticles, produced by thermal annealing from iridium(III) bromide hydrate, is compared when deposited on carbon and titanium(IV) dioxide supports. Samples were investigated using Raman spectroscopy, but due to a small amount of Ir nanoparticles on supports only low intensity bands can appear. It is worth noting that other rare Raman literature (see Introduction) deals with bulk Ir-films/discs with a much larger amount of Ir in samples. Our results show weak bands of Ir-oxide at 548 (E_g) and 719 ($B_{2g} + A_{1g}$) cm^{-1} for the degraded states only. This indicates the degradation of Ir nanoparticles through oxidation on both investigated supports. Structural characteristics of supports and Ir nanoparticles were also investigated using X-ray diffraction and energy-dispersive X-ray spectroscopy. Electrochemical characterization shows that the OER activity of the Ir nanoparticles on carbon is significantly higher than that on TiO_2.

1. Introduction

Electrocatalysis is an important field of application for Ir-based materials. Despite its scarcity and high cost, iridium continues to be intensively researched for its use in proton exchange membrane (PEM) water electrolyzers, which can be used for efficient hydrogen production [1–3]. The main reason for its prevalence is the fact that iridium displays the best compromise between the activity for the oxygen evolution reaction (OER) and stability when water splitting occurs in an acidic environment [4]. Therefore, iridium will remain attractive even though its feedstock is at a critical level and may not be sufficient for practical technological needs [5]. Researchers are looking for an efficient way to reduce the Ir load on electrodes, for example, by using Ir nanoparticles deposited on various suitable supports. Advantageous properties of supported electrocatalysts are (i) high surface area-to-mass ratio, (ii) dispersion of the nanoparticles over the surface of the support, which prevents their aggregation, (iii) higher electrical conductivity and (iv) maximizing the exposed effective catalytic surface area [6].

In addition to the high price and scarcity of Ir, an important disadvantage of OER is also the lack of stable and economical supporting materials at high voltages. The necessary requirements are a large surface area, long-term stability, and sufficiently high electrical conductivity (>0.1 S/cm) [6,7]. Ir-based catalysts have been prepared on various supports such as carbon paper [8], carbon nanotubes [9], self-aligned nanotubes [10], graphene oxide [11,12], antimony-doped tin oxide (ATO) [6,13], $TiON_x$ support [14,15], and TiO_2 [6,16–21]. Carbon materials are reasonably stable under oxygen reduction reaction (ORR) conditions, but not sufficiently stable under severe OER conditions and elevated temperatures. Alternatively, when Ir is used in combination with TiO_2, conductivity becomes a major issue which requires higher loadings of the electrocatalyst. The question remains how to find the best compromise between the high surface area of the support and the amount of Ir required to create a conductive network of nanoparticles [22,23]. Specifically, the supports have a major impact on the long-term stability and functionality of the electrocatalysts.

The literature on mechanisms in various Ir-based materials during OER is extensive [1,2,24], as is the study of supports [6,9,10,13]. Understanding the reasons for Ir instability during OER is crucial for all technological applications. A number of techniques have already been applied to investigate mechanisms, and in our previous work we have

* Corresponding author.
E-mail address: angelja.k.surca@ki.si (A.K. Surca).
[1] On leave from the, Division of Materials Chemistry, Ruđer Bošković Institute, Bijenička 54, 10000 Zagreb, Hrvatska

https://doi.org/10.1016/j.ijhydene.2024.12.337
Received 3 October 2024; Received in revised form 17 December 2024; Accepted 19 December 2024
Available online 23 December 2024

used identical location-TEM (IL-TEM) [25], extended X-ray absorption fine structure (EXAFS),[14] X-ray absorption near edge structure (XANES) and electrochemistry combined with an inductively coupled plasma mass spectrometry (EC-ICP-MS) [3], alternating current (AC) voltammetry [26] and many others to gain insights into the functionality, stability and degradation of Ir-based electrocatalysts and supports. Recently, however, Raman spectroscopy has attracted our attention as it has rarely been used to study Ir-based materials and may still offer much room for important insights into electrocatalytic processes.

Raman spectroscopy is known to provide a vibrational fingerprint of the materials under investigation. In addition, this method is sensitive to the local environment, i.e., it reflects the crystalline and amorphous character of compounds, micro crystallinity, impurities, and defects [27,28]. It is usually characterized as a non-destructive technique and is easy to use for a variety of samples. However, the detection of Raman spectra on dark- or black-colored samples – as often used in electrocatalysis - can be challenging. In Raman measurements, the dark-colored sample can absorb the excitation laser beam, leading to thermal emission and eventually decomposition of the sample. Therefore, the measurement conditions for such samples must be carefully selected to prevent the material from changing, burning or fluorescing due to excessive laser power. Often the signal-to-noise ratio has to be sacrificed to obtain spectra even when the material is measured as a bulk or in the form of a film. Much more questionable is the detection of nanoparticles that are dispersed on the support. A question that appears is how to find a suitable site with enough Ir nanoparticles for the measurement. It is important to note that metallic Ir does not show any experimental bands in the Raman spectra, which means that only eventual oxidation of Ir nanoparticles can be observed, for example, with degradation.

Raman studies found in the literature report on the *in-situ* behavior of electrochemically deposited hydrous IrO_x films [29–32]. They were deposited on Ir foil [30], glassy carbon electrode [32] or roughened Au [29,31]. The Au is roughened to enhance the intensity of the bands in the spectra through the effect of surface-enhanced Raman spectroscopy (SERS). In all these studies, broad overlapping bands were found, which were ascribed to different Ir–O stretching vibrations. Using electrolytes prepared from deuterated water and the isotope ^{18}O, it was suggested that these broad bands mostly belong to the Ir(IV) state, while the band at 602 cm^{-1} [30] (and 608 cm^{-1} [32]) was attributed to Ir(III). These assignations were made according to the work of Huang et al. [33] who reported the Raman vibrations of a rutile IrO_2 single crystal as distinct bands at 145 (B_{1g}), 561 (E_g), 728 (B_{2g}) and 752 (A_{1g}).

In contrast to these mentioned works on Ir-based films [29–32], herein we aim to show – to our knowledge for the first time - whether the Raman spectra of Ir nanoparticles on supports can be detected despite their relatively small amount. Since Ir metals do not have Raman spectra, only oxidation during activation/degradation can be detected. Our measurements are performed directly on the drop-casted samples of Ir nanoparticles on two types of supports, i.e., carbon black (CB - Vulcan) and TiO_2 (P25). Carbon black was chosen as it is the most common support for electrocatalysts in general, even if it is not stable enough under OER conditions. Nonetheless, a feasibility study of Raman spectroscopy of Ir nanoparticles deposited on carbon support might prove useful for other reactions. On the other hand, Ir on TiO_2 is commercially available as an OER catalyst (Umicore). The lack of conductivity of TiO_2 is counterbalanced by a sufficient Ir loading (>40–60 wt%) [17,23,34]. In our experiments, the loading of Ir nanoparticles was lower (21 wt%) than in the commercial catalyst, as the goal was to determine if chemical changes of highly dispersed iridium nanoparticles can be observed with Raman spectroscopy, at the expense of good activity. Two distinctly different supports were also chosen to see whether there was any effect of metal-support interaction. X-ray diffraction (XRD) was used to gain insight into the structure of the samples. Energy dispersive X-ray spectroscopy (EDS) was applied to detect the possible oxidation of metallic Ir nanoparticles synthesized from iridium(III) bromide hydrate. The *ex-situ* Raman spectroelectrochemical experiments in activated and degraded states of CB + Ir and P25+Ir samples were performed to mimic conventional electrocatalytic studies in 0.1 M $HClO_4$(aq) electrolyte.

2. Experimental

2.1. Electrocatalyst preparation

Iridium nanoparticles on TiO_2 (P25) and Vulcan supports were prepared by first dissolving 70 mg of iridium(III) bromide hydrate (Sigma-Aldrich) in 1 mL of MilliQ water (18.2 MΩ cm) at 50 °C. The solutions were then mixed with either 100 mg TiO_2 (P25) (Evonik Industries AG) powder or 130 mg Vulcan XC72 (Cabot) powder (both lightly ground in a mortar) at 50 °C until evaporated. The mixtures were then thermally treated in a 5% H_2/Ar mixture. The temperature was raised to 450 °C at a rate of 2 °C/min and maintained at 450 °C for 1 h. They were then cooled to room temperature at a rate of 3 °C/min. The samples were designated as CB + Ir and P25+Ir. Unsupported Ir nanoparticles were synthesized by thermal annealing of pure iridium(III) bromide hydrate using the same procedure as applied for the synthesis of CB + Ir and P25+Ir.

2.2. Instrumental analysis

A high-resolution X-ray powder diffractometer PANalytical X'Pert PRO MPD (PANalytical B.V., Almelo, The Netherlands) with alpha1 configuration ($CuK_{\alpha1}$ $\lambda = 1.5406$ Å radiation) and a fully open scanning X'Celerator detector was used to perform X-ray diffraction (XRD) measurements. The diffractograms in the 2θ range from 10 to 60° were measured using a step size of 0.034° and an integration time of 100 s. The X'Pert HighScore Plus program was applied to identify the phases together with the PDF-4+ 2021 database of the International Centre for Diffraction Data (ICDD) [35].

The morphology characterization of the samples was investigated by field-emission Zeiss FE-SEM SUPRA TM 35 VP scanning electron microscope (SEM) coupled with an energy dispersive X-ray (EDX) spectrometer with a silicon drift detector EDX Ultim-Max 100 (Oxford Instruments, Oxford, UK). The operating voltage of 7 kV was used for SEM, and 20 kV for SEM/EDX analysis.

The electrochemical treatment of the samples was carried out in a two-compartment, three-electrode cell. The setup was controlled by a potentiostat (ECi-200, Nordic electrochemistry). The samples consisted of an electrocatalyst deposited on a glassy carbon electrode (GCE) mounted as a working electrode in a CTV 101 rotator (Radiometer Analytical). To prepare a homogeneous film, first a 5 mg_{cat}/mL ink was prepared by weighting some of the powdered catalysts and adding the corresponding amount of Milli-Q water. Afterwards, the suspension was in an ultrasonic bath for at least 10 min. Finally, 20 μL of the ink was dropcasted on the GCE. The counter electrode was a carbon rod, and the reference electrode was an Ag/AgCl (BaSi). The latter electrode was placed in the second compartment to avoid contamination with Cl^- ions. The potential of the reference electrode was determined before the experiments with respect to the reversible hydrogen electrode (RHE). The 0.1 M $HClO_4$ electrolyte was prepared by mixing conc. $HClO_4$ (Suprapur 70%, Merck) with Milli-Q water. The electrolyte was saturated with N_2 during all experiments. Both types of samples were first measured in the activated region, i.e. 0.05 to 1.45 V_{RHE}, with 100 cycles at a scan rate of 300 mV/s and 1600 rpm. In the second step, the samples were exposed to a constant current of 2 mA (1 h) at 3600 rpm to force degradation. The degraded-longer samples were first activated and then exposed to 2 mA for 2 h. Details of the electrochemical treatment prior to Raman measurements are given in Table 1. The activity of the samples was measured between 1.2 and 1.6 V_{RHE} for 10 cycles at a scan rate of 10 mV/s. The second cycle is shown. The CVs are corrected based on the capacitive current at 1.2 V_{RHE}. The mass activity was evaluated at 1.6 V vs RHE.

The Raman spectra were recorded on a confocal WITec alpha 300

Table 1
The Ir samples with support, drop-casted onto GCE electrodes, and the conditions used for their activation and degradation.

Sample	State of the sample	Activation/degradation conditions
GCE/P25	GCE/P25	as-deposited (drop-casted)
GCE/ P25+Ir	As-deposited	as-deposited (drop-casted)
	Activated	100 cycles, 300 mV/s, 1600 rpm, 0.05 to 1.45 V_{RHE}
	Degraded	2 mA, 3600 rpm, 1 h
	Degraded-longer (l.)	activated, followed by 2 mA, 2 h
GCE/CB + Ir	As-deposited	as-deposited (drop-casted)
	Activated	100 cycles, 300 mV/s, 1600 rpm, 0.05 to 1.45 V_{RHE}
	Degraded	2 mA, 3600 rpm, 1 h
	Degraded-longer (l.)	activated, followed by 2 mA, 2 h

GCE – glassy carbon electrode; l. – longer; CB – carbon black; P25 – TiO_2.

spectrometer. A green laser light of 532 nm was applied for excitation. Raman spectra of Ir nanoparticles were measured on an Si wafer holder using an integration time (IT) of 1 s and 100 scans, while the laser power was gradually increased from 0.7 mW to 13.6 mW. Pure P25 (TiO_2) suspension was analyzed after drop-casting of an aqueous suspension of P25 to GCE and dried. These Raman spectra were measured using an IT of 0.5 s, 100 scans and laser powers from 1.4 mW to 13.6 mW. *Ex situ* Raman spectra of drop-casted P25+Ir and CB + Ir samples on GCE - as well as the initial drop-casted samples - were measured using a 20× objective, IT = 0.5 s and 100 scans. The laser power was 1.4 mW–1.7 mW. Prior to Raman measurement, the samples were electrochemically treated, carefully cleaned under a stream of MilliQ water, dried and then transferred under the objective of the Raman spectrometer. Several measurements of spectra were taken at distinct locations on the sample.

3. Results and discussion

3.1. Characterization of samples (XRD, EDS, Raman)

XRD patterns of powdered samples P25+Ir and CB + Ir are shown in Fig. 1. The diffraction peaks of P25+Ir (Fig. 1a) are associated with tetragonal TiO_2 (anatase) at angles of 2θ = 25.3° (101), 36.9° (103), 37.8° (004), 38.6° (112), 48.1° (200), 53.9° (105) and 55.1° (211) (PDF 00-021-1272). Tetragonal TiO_2 (rutile) corresponds to diffractions at angles of 2θ = 27.5° (110), 36.1° (101), 54.3° (211), and 56.7° (220) (PDF 01-083-2242). The two broader peaks at 40.7° and 47.3° belong to

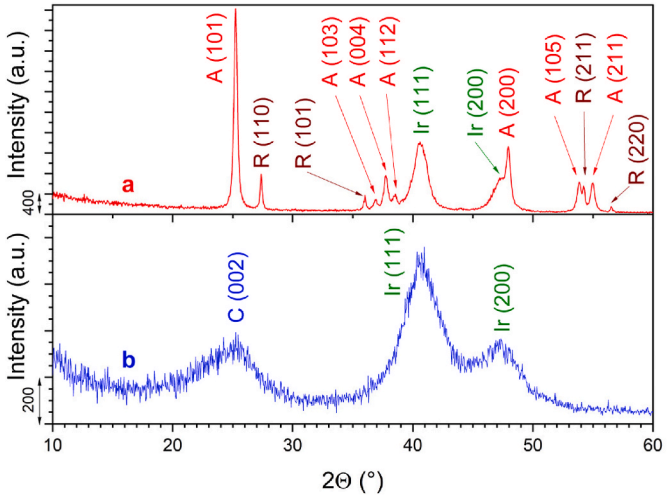

Fig. 1. XRD pattern of the samples: a) P25+Ir and b) CB + Ir.

(111) and (200) diffractions (PDF 04-001-0838) of cubic iridium nanoparticles dispersed over the P25 support.

The XRD pattern showed that not only the anatase phase but also the rutile phase is present in the commercial P25 compound, which is a standard material in the field of photocatalytic reactions. Pure P25 XRD pattern is shown in Fig. S1 in the *Supplementary information*. We calculated the presence of 88 % of anatase and 12 % of rutile phase. The presence of both phases in P25 has already been reported in the literature, but the ratios vary. The most commonly, the ratio of anatase to rutile is reported as 3:1 [36,37], but values such as 85 % anatase and 15 % rutile [38] or 80 % vs. 20 % [39] have also been found. The latter value is given as a bulk concentration, while the reported surface values are 90 % of anatase and 10 % of rutile [39].

The second XRD pattern in Fig. 1b reveals three broad diffraction peaks of the CB + Ir sample. Two peaks are again associated with cubic iridium at diffraction angles of 2θ = 40.7° (111) and 47.3° (200) (PDF 04-001-0838). The third peak corresponds to hexagonal carbon at an angle of 2θ = 25.6° (002) (PDF 04-018-7559). The broad width of both iridium diffractions indicates the nanoparticulate character of iridium. Consequently, we calculated the average particle size on the basis of full width at half the maximum (FWHM) of the peaks in the XRD patterns (Fig. 1). It was found that the iridium nanoparticles are around 7 nm on P25+Ir, and significantly smaller for CB + Ir, with a size of around 2.2 nm. The variation in size is related to the different interaction of iridium with the support material during the synthesis. This could be problematic from the point of view to accurately compare the electrochemical performances, as the activity is related to the number of active sites of iridium, which are more numerous for smaller particles. However, the goal of our study is to investigate the feasibility of Raman spectroscopy to detect supported iridium nanoparticles and thus having different supports, and also different particle size, allows us to screen both parameters.

The Raman spectra of P25 (TiO_2) deposited on GCE reveal similar characteristics of the sample as the XRD patterns. Namely, Raman spectra show predominantly the bands of anatase TiO_2. Its presence is indicated by the bands at 144 (E_g), 197 (E_g), 399 (B_{1g}), 515 (A_{1g}, B_{1g}) and 625 (E_g) cm^{-1} (Fig. 2). Their positions and intensity ratios reflect anatase as described by Ohsaka et al. [40] for its natural mineral. The blue arrows denote the positions of the rutile TiO_2 bands described for single crystal by Porto et al. [41] at 143 cm^{-1} (B_{1g}), 447 cm^{-1} (E_g), 612 cm^{-1} (A_{1g}) and 826 cm^{-1} (B_{2g}). Fig. 2 shows only poorly resolved shoulders at approximately 447 and 612 cm^{-1} (marked with blue arrows), i.e. at positions corresponding to the E_g and A_{1g} modes of the rutile phase. The rutile band at 143 cm^{-1} is overlapped by the very intense mode of the anatase phase. The D and G bands belong to GCE electrode and its Raman spectra are shown in Fig. S2 in the *Supplementary information*.

The Raman spectra were also measured for unsupported Ir nanoparticles (Fig. 3). Namely, Ir nanoparticles were placed on an Si wafer holder to measure the Raman spectrum of our home-made benchmark. It is characteristic of metallic iridium that no bands appear in the Raman spectrum. Indeed, when recording spectra using low laser powers (0.7 mW–1.4 mW), no bands were observed. As the power of the laser beam was further increased, fluorescence gradually began to appear. Simultaneously, bands started to grow at 552 cm^{-1} and 715 cm^{-1}, which increased significantly in intensity at high laser power of 13.6 mW. The positions of these two bands are close to those of the rutile IrO_2 single crystal, as reported by Huang [33]. Specifically, these authors described four allowed first-order active Raman modes: 145 cm^{-1} (B_{1g}), 561 cm^{-1} (E_g), 728 cm^{-1} (B_{2g}) and 752 cm^{-1} (A_{1g}). The first one (145 cm^{-1}) is of very low intensity and is not discernible in our spectra (Fig. 3). The sharp band at 170 cm^{-1} is an instrumental feature that occurs when higher laser powers are applied to reflective substrates (i.e. Si wafer was used as a holder for Ir nanoparticles). The band at 552 cm^{-1} corresponds to the E_g mode and the band at 715 cm^{-1} corresponds to the overlapping B_{2g} and A_{1g} modes of the oxidized Ir-based sample (Fig. 3). The overlap of

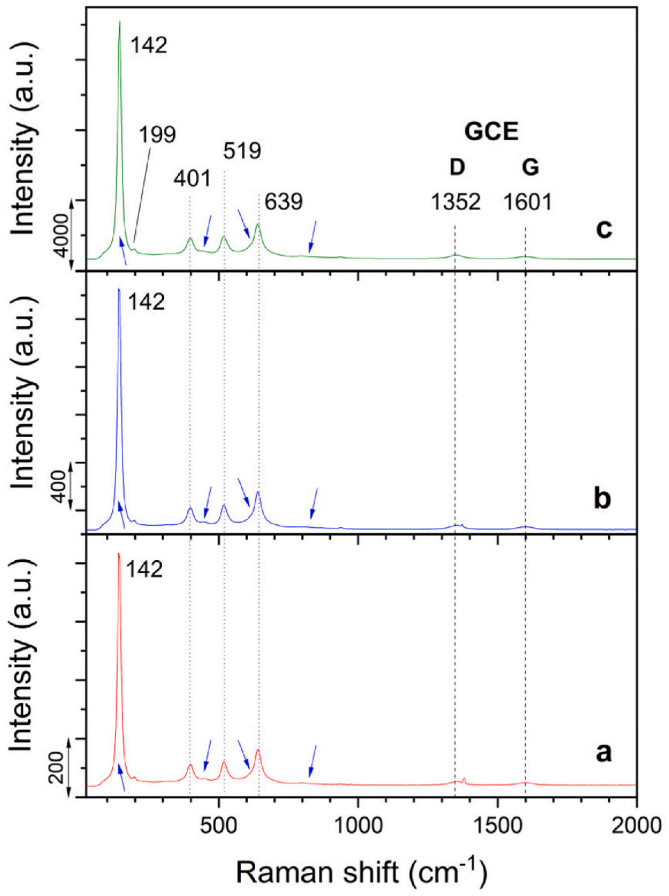

Fig. 2. Raman spectra of P25 (TiO_2) drop-casted on GCE electrode. The spectra were recorded using three different laser powers: a) 1.4 mW, b) 3.0 mW and c) 13.6 mW.

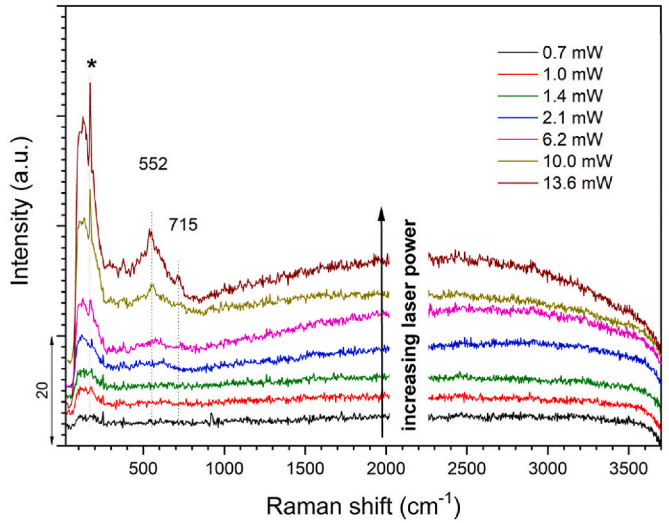

Fig. 3. Raman spectra of Ir nanoparticles. All spectra were recorded at the same position with increasing laser power from 0.7 mW to 13.6 mW * - The sharp band at 170 cm^{-1} is an instrumental feature.

the B_{2g} and A_{1g} modes is not surprising as it has been observed in the as-prepared Ir-based films [42], and IrO_2 deposited on carbon nanotubes [9] or sapphire [43]. The shifts of the bands to lower wavenumbers (552 cm^{-1}, 715 cm^{-1}) relative to the single-crystal values [33] are consistent with the increased disorder [44]. This experiment clearly shows how important is the power of the laser beam as an experimental condition and that the use of too high laser powers can cause the oxidation of Ir nanoparticles.

The prepared Ir nanoparticles were also analyzed using EDS (Fig. 4). Interestingly, this technique showed that the sample consisted of 85.7 at. % iridium and 14.3 at.% oxygen, indicating a partial oxidation of the nanoparticles. However, the O/Ir ratio (0.16) is far from the IrO_2 ratio. Moreover, this amount of oxygen has not yet been noted in the Raman spectra obtained at low laser powers (Fig. 3). Therefore, one can speculate that only the surface is oxidized and the oxidized part formed as an amorphous layer.

3.2. Electrochemical response

The electrochemical activity of Ir-based catalysts is influenced by the degree of oxidation of the outer layer and thus by the activation protocol. In addition, the support can also influence the d-band level of iridium and, consequently, the binding between the active site and the reactants/products of OER. The impact of three different activation protocols on the oxidation of iridium was previously studied with Raman spectroscopy on iridium benchmarks, namely rutile IrO_2 and Ir black nanoparticles [44]. The effects of those three activation protocols were also evaluated on the supported catalysts investigated herein (CB + Ir, P25+Ir), and a complete description can be found in the *Supplementary information* (*Discussion S3*). Briefly, the long-range activation (0.05–1.6 V_{RHE}) was good for CB + Ir but not adequate for P25+Ir, while it was the opposite for the short-range activation (1.1–1.6 V_{RHE}). On the other hand, the activation protocol (0.05–1.45 V_{RHE}) resulted in good activity for both CB + Ir and P25+Ir (Fig. S3).

Afterwards, the activity of the CB + Ir and P25+Ir supported catalysts was recorded after various preparation states, i.e. as-deposited, after activation (0.05–1.45 V_{RHE}), after degradation and after longer degradation (Table 1). It can be observed that the activity is extensively different for the two supported catalysts (Fig. 5 and S3). The profound difference comes from the different particle size of iridium nanoparticles, the nature of supports and their conductivity. Indeed, TiO_2 (P25) powder is not conductive (2×10^{-10} Ω^{-1} cm^{-1}) [45] and thus limits the transport of electrons to the iridium active sites, limiting the efficiency of the reaction. On the other hand, carbon black does not have this issue but lacks the stability under water electrolyser conditions that are used in real devices.

The electrochemical treatment has a similar effect on both investigated catalysts. Namely, the activation protocol boosts the activity of both electrocatalysts, with an increase from 276.8 mA/mg_{Ir} for the as-deposited state to 344.7 mA/mg_{Ir} after the activation for CB + Ir, and an increase from 3.42 mA/mg_{Ir} to 6.66 mA/mg_{Ir} in the case of P25+Ir. This increase is due to the formation of more active hydrous oxides on iridium nanoparticles as observed on the benchmarks [46,47]. Afterwards, a quick degradation test was performed to evaluate how the catalyst would react under intense OER. Therefore, a constant current of 2 mA (around 10 mA/cm^2 as advised for WE testing [48,49]) was applied to the electrode for 1 h and 2 h in two distinctive experiments (degraded and degraded longer). The short time of the experiments was chosen to avoid the burning of the carbon support for CB + Ir and the total passivation of TiO_2 in the case of P25+Ir. At the same time, modification of the iridium under OER conditions such as oxidation or other chemical modification would appear quickly. The goal of the protocol is more focused on observing possible iridium chemical changes than destroying the catalysts. Nonetheless, the short time of the degradation protocol was sufficient to induce reduced activity as observed in Fig. 5. More specifically, the degradation led to a decrease of around 43 % while longer degradation resulted in even lower activity (±80 % decreased activity) in the case of CB + Ir. Similarly, the already low activity of P25+Ir decreases even more after short degradation and longer degradation. Therefore, even the hour-long degradation protocol was sufficient to degrade the catalyst. The degradation can be either

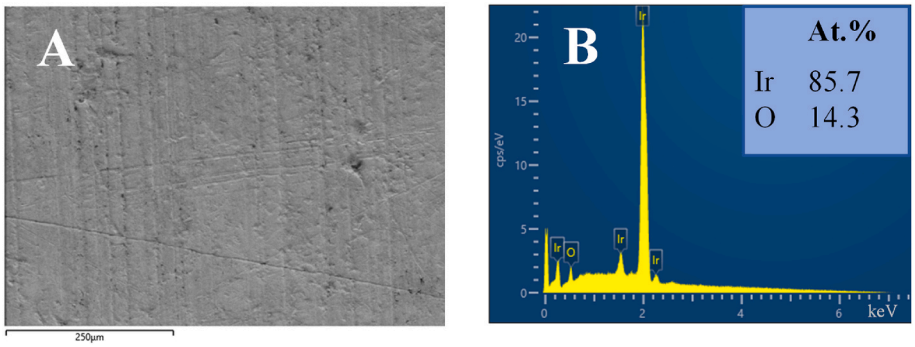

Fig. 4. EDS measurements of Ir nanoparticles. The measurement was performed on the whole visible area of the sample in Fig. 4A.

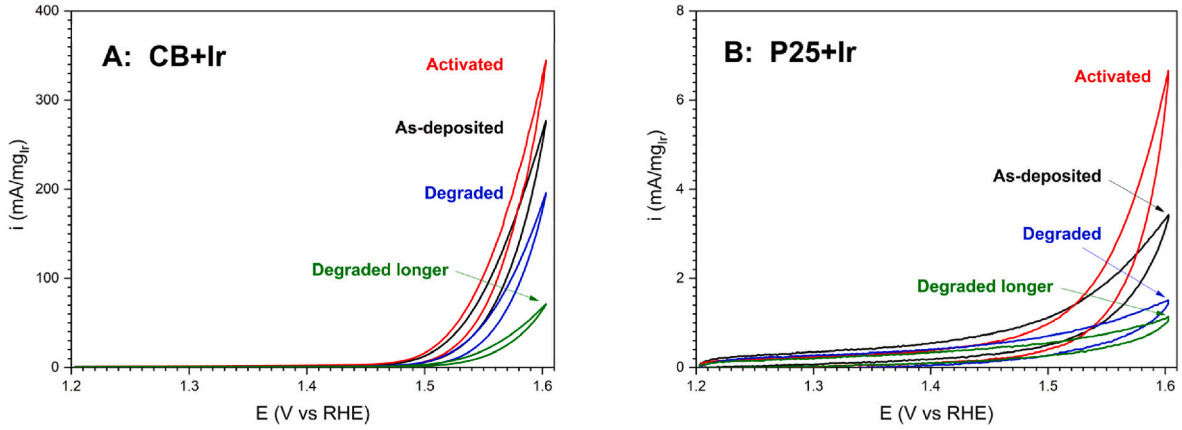

Fig. 5. Activity of (a) CB + Ir and (b) P25+Ir at different stages of electrode treatment.

attributed to the support degradation, iridium dissolution, agglomeration of nanoparticles or formation of less active rutile oxide [46]. Most likely, all the different mechanisms are occurring at the same time and play a role in the decrease of activity. Nonetheless, in our case, some mechanisms are more probable than other. For example, iridium was shown to dissolve following a transient dissolution [50,51] and thus the chosen degradation protocol is unlikely to heavily induce iridium dissolution. Similarly, agglomeration of nanoparticles is unlikely to happen due to support interaction [22], the low loading and the high dispersion of iridium nanoparticles. On the other hand, the support degradation should be carefully considered and could play an important role in the loss of measured activity (further passivation of TiO_2 or carbon degradation). Therefore, the activity was normalized based on the capacitive current to minimize the support degradation impact on the measured activity. Finally, less active oxide can be created during the degradation protocol and their detection, using Raman spectroscopy, is the goal of this study. The overall determination and separation of all the degradation mechanisms (which, most likely, are all happening to a different level) would require extensive investigation. Hereby, we focused on what process can be detected using Raman spectroscopy on as-prepared, activated, degraded and degraded longer states (Table 1).

3.3. Ex situ Raman measurements

The aim of this study is to check whether it is possible to obtain any formation of Ir oxide after activation and degradation of the P25+Ir and CB + Ir samples using Raman spectroscopy. The challenge is whether we can detect spectra of Ir nanoparticles dispersed on the support and due to low amount of iridium. Since the Ir metal has no Raman bands, only its conversion to Ir oxide after activation or degradation could be detected. In contrast to this work on Ir nanoparticles, the previous Raman studies were carried out on electrochemically deposited IrO_x films [29–32].

The P25+Ir and CB + Ir samples were activated and degraded according to the protocols in Table 1. After each electrochemical treatment, the Raman spectra were recorded at different locations on the

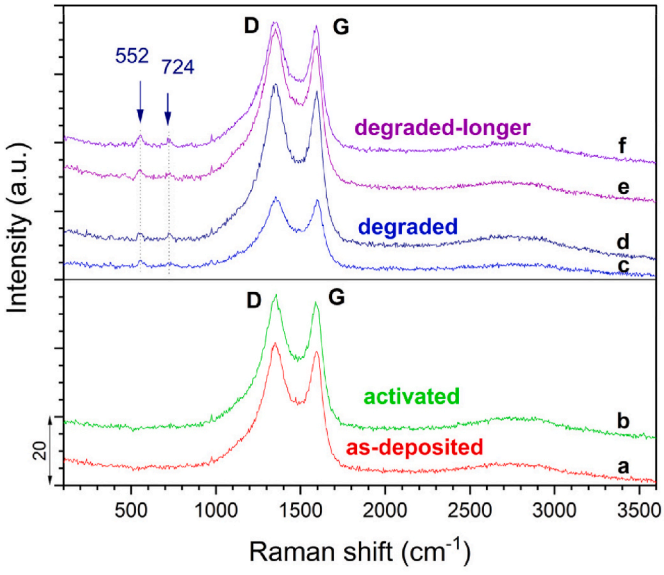

Fig. 6. Raman spectra of Ir black on CB support, deposited on the GCE electrode: a) as-deposited, b) activated, c,d) degraded and e,f) degraded-longer states. The measurements were performed using a laser power of 1.4 mW (a–c), 1.6 mW (d) and 1.7 mW (e,f). The spectra (a,b,e,f) were measured at different locations, while the spectra (c,d) were recorded at the same location.

sample (Figs. 6 and 7). Both examples differ considerably, as the Raman bands of the Ir oxide do not overlap with the bands of CB support (Fig. 6), while they overlap considerably with the modes of P25 (Fig. 7).

Accordingly, the Raman spectra of the GCE/CB + Ir sample were recorded in the as-deposited and activated states at different locations but showed no presence of IrO_2 bands (Fig. 6). Several hypotheses can be advanced to explain the absence of IrO_2 bands. It could be due to Ir nanoparticles remaining in the elemental form after activation, which does not provide Raman spectrum. However, this would not explain the increase in activity. Therefore, one can speculate that the Ir oxide is missing precisely at these measurement locations, or its concentration is insufficient to be detected. Anyway, when we further examined the degraded and the degraded-longer samples (Table 1), the low intensity bands at 552 and 724 cm^{-1} were observed (Fig. 6). These bands can be ascribed to IrO_2 [33]. Their intensity is quite low, and with the aim of increasing them somewhat, the laser power was enlarged slightly, although we were approaching the range of laser power that can cause oxidation of Ir to IrO_2 (Fig. 3). However, even such an increase in laser power did not contribute to an appreciable increase in the intensity of the 552 and 724 cm^{-1} bands. This indicates that the IrO_2 content at each measured location was relatively low. We have to add at this point that IrO_2 bands were detected in the spectra shown in Fig. 6, whereas at many other locations studied these bands were not observed. This is not surprising since the CB + Ir sample contains 17 wt% Ir. Nonetheless, this could indicate that the decrease in activity observed after degradation (Fig. 5, Table 1) can partially be attributed to a change in intrinsic iridium activity. Namely, iridium oxidizes to the more stable, but less active, rutile-type structure.

In the case of the second support, the bands of IrO_2 overlap with the bands of P25 (TiO_2) (Fig. 7). As mentioned above, the bands of support P25 mainly show the presence of the anatase phase (Fig. 2) [40], which is reported as its main component [36–38]. The anatase bands dominate the spectra of the GCE/P25+Ir sample in the as-deposited and activated states in Fig. 7Aa,b. The shoulders appearing at the positions of the rutile bands are practically not visible (marked with blue arrows), which is probably also due to the presence of 21 wt% Ir nanoparticles on the surface of the TiO_2 particles. However, the most intense E_g band of anatase shifted from 142 cm^{-1} in the spectrum of GCE/P25 (Fig. 2) to 146 cm^{-1} in the spectrum of GCE/P25+Ir sample in the as-deposited, activated and some of degraded states (Fig. 7Aa-d). Such a blue shift of the TiO_2 E_g band has already been described in the spectra of TiO_2 nanoparticles coated with dodecyl benzenesulfonic acid or stearic acid, i.e. due to the presence of the coating [52]. Similarly, our P25+Ir samples exhibit Ir nanoparticles on the surface of TiO_2, which may be a reason for a similar blue shift. With the increase in laser power (Fig. 7, scan c-f), this E_g band shifted further to 151 cm^{-1}, which – together with the increase in intensity of the 612 cm^{-1} – may indicate the conversion of a small portion of anatase to rutile.

In addition, we can examine the GCE/P25+Ir spectra (Fig. 7) with regard to the possible formation of IrO_2. No IrO_2 could be noted in the spectra of as-deposited and activated states, so, only one representative spectrum is shown for each state (Fig. 7Aa,b). As we began to slightly increase the laser power for degraded states, the shoulder bands of IrO_2 at 552 and 724 cm^{-1} started to appear (Fig. 7Ac-f). They are indicated by vertical black arrows. At an even more aggressive degradation (labeled as degraded-longer in Table 1), very little sample remained at the GCE electrodes and Raman measurement was impossible. Anyhow, the Raman measurements of Ir nanoparticles on two different supports revealed that the presence of a very low amount of IrO_2 can be detected after degradation. However, such measurements are tedious and time-consuming since spectra need to be recorded at numerous locations to get a good overview of the electrocatalyst sample in the case of low iridium nanoparticles loading.

3.4. Conclusions

Ir nanoparticles synthesized from iridium(III) bromide hydrate exhibited a small amount of amorphous Ir oxide, as evidenced by EDS analysis. The possibility of Raman spectroscopy to detect eventual changes of Ir nanoparticles on carbon black (CB) or P25 (TiO_2) supports was evaluated next. The metallic Ir is Raman inactive, while IrO_2 has characteristic Raman modes at 752 (A_{1g}), 728 (B_{2g}) and 561 (E_g) [33]. It was found that IrO_2 modes were not present in the samples in the as-deposited and activated states. However, IrO_2 was detected at certain locations for degraded states for either CB + Ir or P25+Ir. The stability of the Ir nanoparticles under a green 532 nm laser was also tested. This revealed that increasing the laser power leads to oxidation to Ir oxide. Caution is therefore needed with such measurements.

The activity of iridium towards OER is highly related to its oxidation state. Therefore, the activation protocol and surface modification during the reaction are of primordial importance. Hereby, we have shown that Raman spectroscopy can help to uncover the oxidation of iridium, even when in the form of nanoparticles highly dispersed on two different supports. More specifically, the formation of Ir oxide could be observed

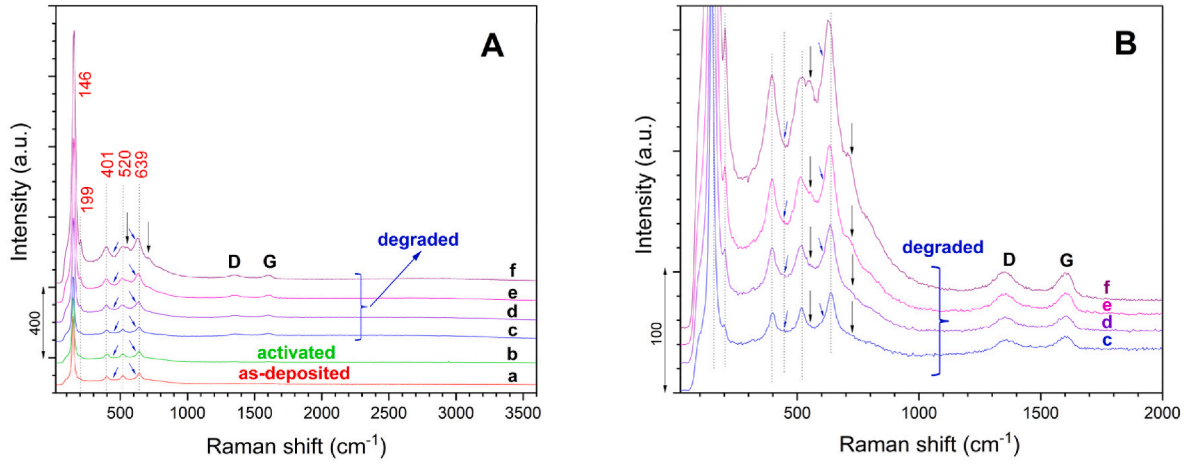

Fig. 7. Raman spectra of Ir black on P25 (TiO_2) support, deposited on the GCE electrode, in spectral range: A) 20–3600 cm^{-1} and B) 20–2000 cm^{-1} and for a) as-deposited, b) activated, c-f) degraded states. The measurements were performed using a laser power of 1.4 mW (a–c), 1.5 mW (d), 1.7 mW (e) and 1.9 mW (f). The spectra (a–c) were measured at different locations, while the spectra (c–f) were obtained at the same location. The dotted lines indicate the anatase bands. The blue arrows depict the positions of the rutile bands. The vertical black arrows indicate the bands of IrO_2. (For interpretation of the references to color in this figure legend, the reader is referred to the Web version of this article.)

on both samples, CB + Ir and P25+Ir, after conducting degradation procedures, relevant to water electrolyser conditions. However, combination with other techniques such as online-ICP-MS (for dissolution studies) or TEM (observation of degradation) are suggested to discern the complete story of iridium degradation.

CRediT authorship contribution statement

Leonard Moriau: Writing – review & editing, Writing – original draft, Investigation, Data curation, Conceptualization. **Ivan Marić:** Investigation, Data curation. **Marjan Bele:** Investigation, Data curation. **Anja Logar:** Investigation. **Nejc Hodnik:** Writing – review & editing, Funding acquisition. **Angelja K. Surca:** Writing – review & editing, Writing – original draft, Investigation, Funding acquisition, Data curation, Conceptualization.

Declaration of competing interest

The authors declare that they have no known competing financial interests or personal relationships that could have appeared to influence the work reported in this paper.

Acknowledgements

This study was funded by the Slovenian Research Agency through the research program P2-0393, infrastructure program I0–0003 and projects J1-4401, N2-0155 and N2-0248. Authors further acknowledge funding from the European Research Council (ERC) Starting Grant 123STABLE (Grant Agreement ID: 852208) and NATO Science for Peace and Security Program (Grant G6230).

Appendix A. Supplementary data

Supplementary data to this article can be found online at https://doi.org/10.1016/j.ijhydene.2024.12.337.

References

[1] Abbott DF, Lebedev D, Waltar K, Povia M, Nachtegaal M, Fabbri E, Copéret C, Schmidt TJ. Iridium oxide for the oxygen evolution reaction: correlation between particle size, morphology, and the surface hydroxo layer from operando XAS. Chem Mater 2016;28:6591–604. https://doi.org/10.1021/acs.chemmater.6b02625.

[2] Cherevko S, Geiger S, Kasian O, Mingers A, Mayrhofer KJJ. Oxygen evolution activity and stability of iridium in acidic media. Part 1. – metallic iridium. J Electroanal Chem 2016;773:69–78. https://doi.org/10.1016/j.jelechem.2016.04.033.

[3] Jovanovič P, Hodnik N, Ruiz-Zepeda F, Arčon I, Jozinović B, Zorko M, Bele M, Šala M, Šelih VS, Hočevar S, Gaberšček M. Electrochemical dissolution of iridium and iridium oxide particles in acidic media: transmission electron microscopy, electrochemical flow cell coupled to inductively coupled plasma mass spectrometry, and X-ray absorption spectroscopy study. J Am Chem Soc 2017;139:12837–46. https://doi.org/10.1021/jacs.7b08071.

[4] Reier T, Oezaslan M, Strasser P. Electrocatalytic oxygen evolution reaction (OER) on Ru, Ir, and Pt catalysts: a comparative study of nanoparticles and bulk materials. ACS Catal 2012;2:1765–72. https://doi.org/10.1021/cs3003098.

[5] Minke C, Suermann M, Bensmann B, Hanke-Rauschenbach R. Is iridium demand a potential bottleneck in the realization of large-scale PEM water electrolysis? Int J Hydrogen Energy 2021;46:23581–90. https://doi.org/10.1016/j.ijhydene.2021.04.174.

[6] Han B, Risch M, Belden S, Lee S, Bayer D, Mutoro E, Shao-Horn Y. Screening oxide support materials for OER catalysts in acid. J Electrochem Soc 2018;165:F813–20. https://doi.org/10.1149/2.0921810jes.

[7] Marshall A, Børresen B, Hagen G, Tsypkin M, Tunold R. Preparation and characterisation of nanocrystalline IrxSn1−xO2 electrocatalytic powders. Mater Chem Phys 2005;94:226–32. https://doi.org/10.1016/j.matchemphys.2005.04.039.

[8] Lee B-S, Park H-Y, Cho MK, Jung JW, Kim H-J, Henkensmeier D, Yoo SJ, Kim JY, Park S, Lee K-Y, Jang JH. Development of porous Pt/IrO2/carbon paper electrocatalysts with enhanced mass transport as oxygen electrodes in unitized regenerative fuel cells. Electrochem Commun 2016;64:14–7. https://doi.org/10.1016/j.elecom.2016.01.002.

[9] Chen YM, Chen CA, Huang YS, Lee KY, Tiong KK. Synthesis of IrO2 nanocrystals on carbon nanotube bundle arrays and their field emission characteristics. J Alloys Compd 2009;487:659–64. https://doi.org/10.1016/j.jallcom.2009.07.181.

[10] Chen R-S, Huang Y-S, Tsai D-S, Chattopadhyay S, Wu C-T, Lan Z-H, Chen K-H. Growth of well aligned IrO_2 nanotubes on $LiTaO_3$ (012) substrate. Chem Mater 2004;16:2457–62. https://doi.org/10.1021/cm030668n.

[11] Kong F-D, Zhang S, Yin G-P, Liu J, Xu Z-Q. IrO2-graphene hybrid as an active oxygen evolution catalyst for water electrolysis. Int J Hydrogen Energy 2013;38:9217–22. https://doi.org/10.1016/j.ijhydene.2013.05.023.

[12] Wu X, Feng B, Li W, Niu Y, Yu Y, Lu S, Zhong C, Liu P, Tian Z, Chen L, Hu W, Li CM. Metal-support interaction boosted electrocatalysis of ultrasmall iridium nanoparticles supported on nitrogen doped graphene for highly efficient water electrolysis in acidic and alkaline media. Nano Energy 2019;62:117–26. https://doi.org/10.1016/j.nanoen.2019.05.034.

[13] Puthiyapura VK, Mamlouk M, Pasupathi S, Pollet BG, Scott K. Physical and electrochemical evaluation of ATO supported IrO2 catalyst for proton exchange membrane water electrolyser. J Power Sources 2014;269:451–60. https://doi.org/10.1016/j.jpowsour.2014.06.078.

[14] Moriau L, Bele M, Marinko Ž, Ruiz-Zepeda F, Koderman Podboršek G, Šala M, Šurca AK, Kovač J, Arčon I, Jovanovič P, Hodnik N, Suhadolnik L. Effect of the morphology of the high-surface-area support on the performance of the oxygen-evolution reaction for iridium nanoparticles. ACS Catal 2021;11:670–81. https://doi.org/10.1021/acscatal.0c04741.

[15] Bele M, Stojanovski K, Jovanovič P, Moriau L, Koderman Podboršek G, Moškon J, Umek P, Sluban M, Dražič G, Hodnik N, Gaberšček M. Towards stable and conductive titanium oxynitride high-surface-area support for iridium nanoparticles as oxygen evolution reaction electrocatalyst. ChemCatChem 2019;11:5038–44. https://doi.org/10.1002/cctc.201901487.

[16] Reier T, Teschner D, Lunkenbein T, Bergmann A, Selve S, Kraehnert R, Schlögl R, Strasser P. Electrocatalytic oxygen evolution on iridium oxide: uncovering catalyst-substrate interactions and active iridium oxide species. J Electrochem Soc 2014;161:F876–82. https://doi.org/10.1149/2.0411409jes.

[17] Oakton E, Lebedev D, Povia M, Abbott DF, Fabbri E, Fedorov A, Nachtegaal M, Copéret C, Schmidt TJ. IrO_2-TiO_2 : a high-surface-area, active, and stable electrocatalyst for the oxygen evolution reaction. ACS Catal 2017;7:2346–52. https://doi.org/10.1021/acscatal.6b03246.

[18] Zhang K, Guo C, Wu Y, Yao R, Zhao Q, Li J, Liu G. Amorphous iridium oxide coating on TiO2 for efficient electrocatalytic oxygen evolution reaction. Int J Hydrogen Energy 2024;69:1105–12. https://doi.org/10.1016/j.ijhydene.2024.05.114.

[19] Lin Y, Wu B, Chen A, Su J, Chen L. Iridium-titanium oxides for efficient oxygen evolution reaction in acidic media. Int J Hydrogen Energy 2023;48:10368–76. https://doi.org/10.1016/j.ijhydene.2022.11.348.

[20] Pham CV, Bühler M, Knöppel J, Bierling M, Seeberger D, Escalera-López D, Mayrhofer KJJ, Cherevko S, Thiele S. IrO2 coated TiO2 core-shell microparticles advance performance of low loading proton exchange membrane water electrolyzers. Appl Catal B Environ 2020;269:118762. https://doi.org/10.1016/j.apcatb.2020.118762.

[21] Cheng J, Yang J, Kitano S, Juhasz G, Higashi M, Sadakiyo M, Kato K, Yoshioka S, Sugiyama T, Yamauchi M, Nakashima N. Impact of Ir-valence control and surface nanostructure on oxygen evolution reaction over a highly efficient Ir–TiO_2 nanorod catalyst. ACS Catal 2019;9:6974–86. https://doi.org/10.1021/acscatal.9b01438.

[22] Moriau L, Smiljanić M, Lončar A, Hodnik N. Supported iridium-based oxygen evolution reaction electrocatalysts - recent developments. ChemCatChem 2022;14:e202200586. https://doi.org/10.1002/cctc.202200586.

[23] Puthiyapura VK, Pasupathi S, Su H, Liu X, Pollet B, Scott K. Investigation of supported IrO2 as electrocatalyst for the oxygen evolution reaction in proton exchange membrane water electrolyser. Int J Hydrogen Energy 2014;39:1905–13. https://doi.org/10.1016/j.ijhydene.2013.11.056.

[24] Schweinar K, Gault B, Mouton I, Kasian O. Lattice oxygen exchange in rutile IrO_2 during the oxygen evolution reaction. J Phys Chem Lett 2020;11:5008–14. https://doi.org/10.1021/acs.jpclett.0c01258.

[25] Bele M, Podboršek GK, Lončar A, Jovanovič P, Hrnjić A, Marinko Ž, Kovač J, Surca AK, Kamšek AR, Dražić G, Hodnik N, Suhadolnik L. *Nano lab* ” advanced characterization platform for studying electrocatalytic iridium nanoparticles dispersed on TiO *x N y supports Prepared on Ti transmission electron microscopy grids*. ACS Appl Nano Mater 2023;6:10421–30. https://doi.org/10.1021/acsanm.3c01368.

[26] Vodeb O, Lončar A, Bele M, Hrnjić A, Jovanovič P, Gaberšček M, Hodnik N. Intrinsic properties of nanoparticulate Ir-based catalysts for oxygen evolution reaction by AC voltammetry. Electrochim Acta 2023;464:142882. https://doi.org/10.1016/j.electacta.2023.142882.

[27] Liao PC, Chen CS, Ho WS, Huang YS, Tiong KK. Characterization of IrO2 thin films by Raman spectroscopy. Thin Solid Films 1997;301:7–11. https://doi.org/10.1016/S0040-6090(96)09545-4.

[28] Xu Z, He Z, Song Y, Fu X, Rommel M, Luo X, Hartmaier A, Zhang J, Fang F. Topic review: application of Raman spectroscopy characterization in micro/nano-machining. Micromachines 2018;9:361. https://doi.org/10.3390/mi9070361.

[29] Mo Y, Stefan IC, Cai W-B, Dong J, Carey P, Scherson DA. In situ iridium L III -edge X-ray absorption and surface enhanced Raman spectroscopy of electrodeposited iridium oxide films in aqueous electrolytes. J Phys Chem B 2002;106:3681–6. https://doi.org/10.1021/jp014452p.

[30] Pavlovic Z, Ranjan C, Gao Q, Van Gastel M, Schlögl R. Probing the structure of a water-oxidizing anodic iridium oxide catalyst using Raman spectroscopy. ACS Catal 2016;6:8098–105. https://doi.org/10.1021/acscatal.6b02343.

[31] Pavlovic Z, Ranjan C, Van Gastel M, Schlögl R. The active site for the water oxidising anodic iridium oxide probed through in situ Raman spectroscopy. Chem Commun 2017;53:12414–7. https://doi.org/10.1039/C7CC05669A.

[32] Saeed KH, Forster M, Li J-F, Hardwick LJ, Cowan AJ. Water oxidation intermediates on iridium oxide electrodes probed by in situ electrochemical SHINERS. Chem Commun 2020;56:1129–32. https://doi.org/10.1039/C9CC08284K.
[33] Huang YS, Lin SS, Huang CR, Lee MC, Dann TE, Chien FZ. Raman spectrum of IrO2. Solid State Commun 1989;70:517–22. https://doi.org/10.1016/0038-1098(89)90942-3.
[34] Fuentes RE, Colón-Mercado HR, Martínez-Rodríguez MJ. Pt-Ir/TiC electrocatalysts for PEM fuel cell/electrolyzer process. J Electrochem Soc 2014;161:F77–82. https://doi.org/10.1149/2.050401jes.
[35] Gates-Rector S, Blanton T. The powder diffraction file: a quality materials characterization database. Powder Diffr 2019;34:352–60. https://doi.org/10.1017/S0885715619000812.
[36] Han E, Vijayarangamuthu K, Youn J, Park Y-K, Jung S-C, Jeon K-J. Degussa P25 TiO 2 modified with H 2 O 2 under microwave treatment to enhance photocatalytic properties. Catal Today 2018;303:305–12. https://doi.org/10.1016/j.cattod.2017.08.057.
[37] Ohno T, Sarukawa K, Tokieda K, Matsumura M. Morphology of a TiO2 photocatalyst (degussa, P-25) consisting of anatase and rutile crystalline phases. J Catal 2001;203:82–6. https://doi.org/10.1006/jcat.2001.3316.
[38] Qin X, Jing L, Tian G, Qu Y, Feng Y. Enhanced photocatalytic activity for degrading Rhodamine B solution of commercial Degussa P25 TiO2 and its mechanisms. J Hazard Mater 2009;172:1168–74. https://doi.org/10.1016/j.jhazmat.2009.07.120.
[39] Andriopoulou C, Boghosian S. Tuning the configuration of dispersed oxometallic sites in supported transition metal oxide catalysts: a temperature dependent Raman study. Catal Today 2019;336:74–83. https://doi.org/10.1016/j.cattod.2019.01.080.
[40] Ohsaka T, Izumi F, Fujiki Y. Raman spectrum of anatase, TiO 2. J Raman Spectrosc 1978;7:321–4. https://doi.org/10.1002/jrs.1250070606.
[41] Porto SPS, Fleury PA, Damen TC. Raman spectra of Ti O 2 , Mg F 2 , Zn F 2 , Fe F 2 , and Mn F 2. Phys Rev 1967;154:522–6. https://doi.org/10.1103/PhysRev.154.522.
[42] Liao PC, Huang YS, Tiong KK. Characterization of RuO2 and IrO2 films deposited on Si substrate. J Alloys Compd 2001:98–102. https://doi.org/10.1016/S0925-8388(00)01403-1. 317–318.
[43] Korotcov AV, Huang Y-S, Tsai D-S, Tiong K-K. Raman scattering characterization of vertical aligned 1D IrO2 nanocrystals grown on single crystal oxide substrates. Solid State Commun 2006;137:310–4. https://doi.org/10.1016/j.ssc.2005.11.038.
[44] Moriau L, Nazrulla MA, Logar A, Pavko L, Bele M, Hodnik N, Surca AK. Ir metal nanoparticles and IrO2 for acidic oxygen evolution reaction: insight from Raman spectroscopy. Sustainable Materials and Technologies 2024;40:e00901. https://doi.org/10.1016/j.susmat.2024.e00901.
[45] Moskon J, Dominko R, Gaberscek M, Cerc-Korosec R, Jamnik J. Citrate-derived carbon nanocoatings for poorly conducting cathode. J Electrochem Soc 2006;153:A1805. https://doi.org/10.1149/1.2221864.
[46] Minguzzi A, Locatelli C, Lugaresi O, Achilli E, Cappelletti G, Scavini M, Coduri M, Masala P, Sacchi B, Vertova A, Ghigna P, Rondinini S. Easy accommodation of different oxidation states in iridium oxide nanoparticles with different hydration degree as water oxidation electrocatalysts. ACS Catal 2015;5:5104–15. https://doi.org/10.1021/acscatal.5b01281.
[47] Danilovic N, Subbaraman R, Chang KC, Chang SH, Kang Y, Snyder J, Paulikas AP, Strmcnik D, Kim YT, Myers D, Stamenkovic VR, Markovic NM. Using surface segregation to design stable Ru-Ir oxides for the oxygen evolution reaction in acidic environments. Angew Chem Int Ed 2014;53:14016–21. https://doi.org/10.1002/anie.201406455.
[48] McCrory CCL, Jung S, Peters JC, Jaramillo TF. Benchmarking heterogeneous electrocatalysts for the oxygen evolution reaction. J Am Chem Soc 2013;135:16977–87. https://doi.org/10.1021/ja407115p.
[49] Walter MG, Warren EL, McKone JR, Boettcher SW, Mi Q, Santori EA, Lewis NS. Solar water splitting cells. Chem Rev 2010;110:6446–73. https://doi.org/10.1021/cr1002326.
[50] Cherevko S, Zeradjanin AR, Topalov AA, Kulyk N, Katsounaros I, Mayrhofer KJJ. Dissolution of noble metals during oxygen evolution in acidic media. ChemCatChem 2014;6:2219–23. https://doi.org/10.1002/cctc.201402194.
[51] Cherevko S, Geiger S, Kasian O, Mingers A, Mayrhofer KJJ. Oxygen evolution activity and stability of iridium in acidic media. Part 2. – electrochemically grown hydrous iridium oxide. J Electroanal Chem 2016;774:102–10. https://doi.org/10.1016/j.jelechem.2016.05.015.
[52] Xu CY, Zhang PX, Yan L. Blue shift of Raman peak from coated TiO 2 nanoparticles. J Raman Spectrosc 2001;32:862–5. https://doi.org/10.1002/jrs.773.